How to cite: *Angew. Chem. Int. Ed.* **2025**, e202513556
doi.org/10.1002/anie.202513556

MOF Water Oxidation Catalysts

Fe-Triazolate Metal–Organic Frameworks as Water Oxidation Catalysts with Dual Photoanode Functionality

*Jully Patel[+], Naduvile Purayil Dileep[+], Vladimir Bondar, Priya Gopal, Anton V. Sinitskiy, Sergei Savikhin, and Yulia Pushkar**

Abstract: Artificial photosynthesis is an emerging technology that achieves renewable fuels, such as hydrogen, from sunlight. Its realization depends on finding highly active and stable catalysts of water splitting and photoactive materials for light absorption. To be scalable, these should contain only abundant elements. Here, for the first time, Fe-triazolate ($Fe(ta)_2$) and its metal substituted derivatives (Fe-Metal$(ta)_2$) Metal-organic frameworks (MOFs) are characterized as new dual-function materials for photo-absorption and water oxidation catalysis in acidic media. The materials were studied by a range of structural, spectroscopic, and computational density functional theory (DFT) techniques. $Fe(ta)_2$ and Fe-$Mn(ta)_2$ were found to be highly active and stable in chemical and photochemical water oxidation, and in addition function as photoanodes, with photo-electrocatalytic currents ($\sim$2.00 x 10^{-3} Acm^{-2} at + 1.4 V vs. Ag/AgCl) at $pH = 1$. The possibility of a unique catalytic mechanism where O—O bond formation is possible from the coupling of two adjacent $Fe^{IV} = O$ fragments was demonstrated by DFT analysis. Thus, Fe-triazolate MOF has been established as a new, stable, scalable, versatile, and efficient platform for sustainable energy conversion in the realm of artificial photosynthesis.

The present environmental scenario necessitates an urgent transition towards cleaner energy sources. Harnessing sunlight through artificial photosynthesis is one of the most effective approaches to generating carbon-neutral, environmentally acceptable fuel (i.e., hydrogen).[1] Further development of artificial photosynthesis requires the discovery of economically viable, large-scale hydrogen production from light-driven water splitting with earth abundant materials (i.e., iron or Photosystem II mimicking Mn-based system). The efficient realization of this approach requires that light absorption, charge separation, and catalysis happen efficiently. The biggest challenge is to develop stable, efficient photoanodes for water oxidation reaction that are based on earth-abundant metals and are economically viable. Most photoanodes are realized with two distinct components: a photo-absorbing material, often a semiconductor stable in an electrolyte environment, and a catalyst.[2] In a natural system such as Photosystem II, these functions are also separated between the chlorophyll molecules for light absorption and the oxygen-evolving complex for water oxidation catalysis.[3] Following this logic, we recently demonstrated a photoanode based on $[Ru(tpy)(Qc)(H_2O)]^+$ (tpy = 2,2′:6′,2″-terpyridine and Qc = 8-quinoline carboxylate) water oxidation catalyst integrated into photoactive Fe-based MIL-142 MOF, demonstrating $\sim$1.6 x 10^{-3} Acm^{-2} in photo-electrocatalytic water splitting at $pH = 1$ with visible light and + 1.4 V versus Ag/AgCl bias.[4] Demonstrating a comparable performance with only earth-abundant elements in the MOF or any other type of material while avoiding using precious metal and complex synthesis should constitute a significant advancement. Hematite (Fe_2O_3) has been widely studied for photoanode applications, but significant limitations of this material are now well recognized, such as low charge mobility, low catalytic activity, and lack of stability in acidic electrolytes, most favorable for proton-conducting polymer technology.[5]

MOFs allow for a complex structural design with variation in metal coordination environments, and a revolutionary development can occur when a single material demonstrates dual functionality, absorbing light and catalyzing electrochemical reactions.[6–10] In addition, the unification of both light-absorbing and catalytic functions in a single material can significantly lower the production cost of the artificial photosynthesis device. Felipe Gandara et al. reported a family of metal-triazole MOFs using triazolate and its derivatives as linkers and divalent metals like Mg, Mn, Fe, Co, Cu, and Zn (Figure 1a).[8–10] Due to the ability to connect multiple metal sites and its ease of modification, the triazolate and its derivatives stand out as an attractive ligand for designing new MOFs.[6,7] Here, we discovered that Fe and mixed Fe-Mn-triazolate MOF ($Fe(ta)_2$, Fe-$Mn(ta)_2$) (Figure 1a) are stable in acidic media and highly active

[*] J. Patel[+], N. P. Dileep[+], V. Bondar, S. Savikhin, Y. Pushkar
Department of Physics and Astronomy, Purdue University, West Lafayette IN 47907, USA
E-mail: ypushkar@purdue.edu
P. Gopal, A. V. Sinitskiy
ML LC, Southborough, MA 01772, USA
[+] Both authors contributed equally to this work.

Additional supporting information can be found online in the Supporting Information section

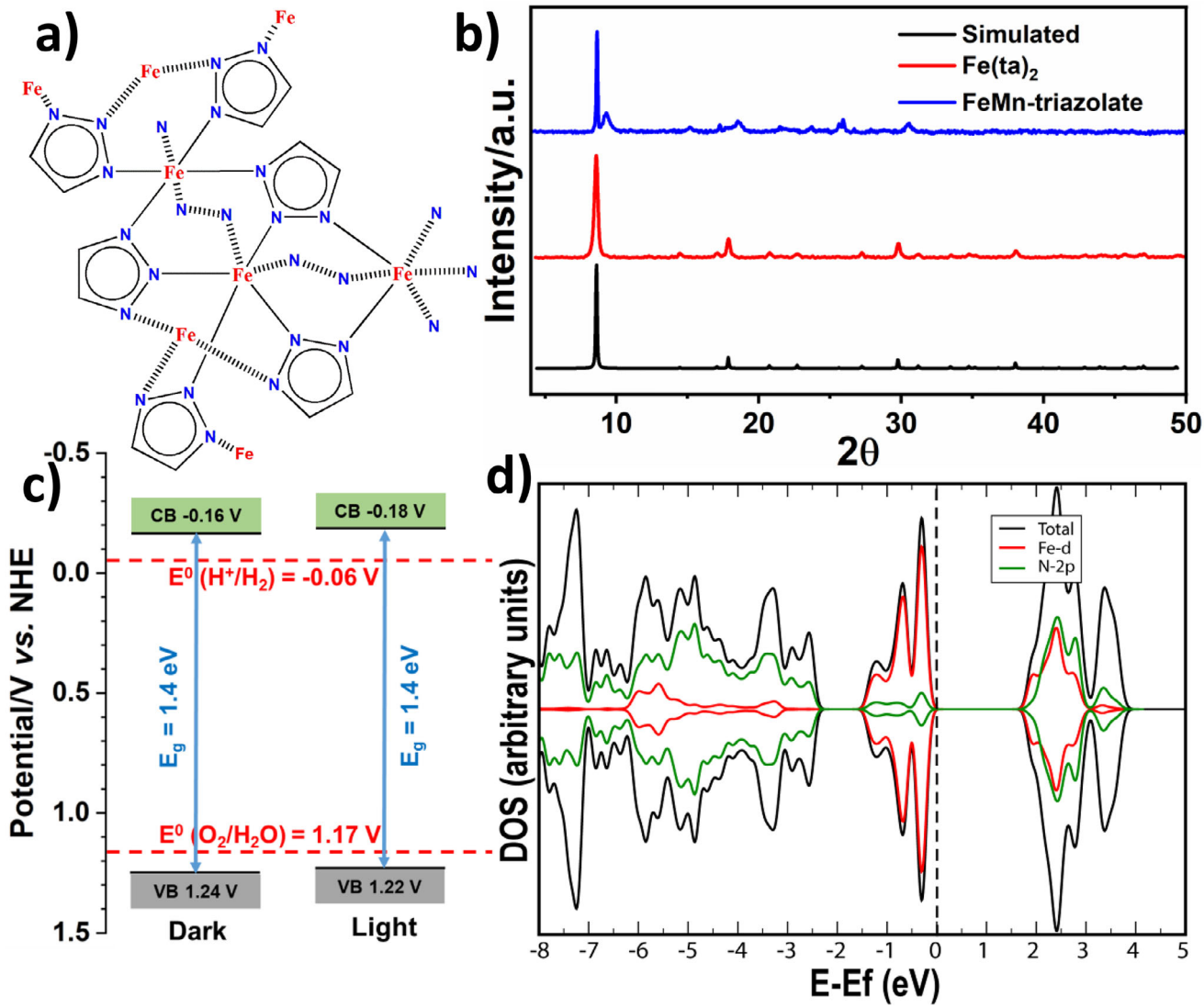

Figure 1. a) Structure of $Fe(ta)_2$, b) XRD pattern of $Fe(ta)_2$ and Fe-$Mn(ta)_2$ with the corresponding simulated pattern. c) Band position of $Fe(ta)_2$ without and with light. The required potential for the HER or OER versus NHE at $pH = 1$ is marked in the figure, and d) Density of states for the $Fe(ta)_2$ crystal predicted by DFT.

in chemical and photochemical water oxidation catalysis. Moreover, photoanodes based on these materials oxidize water in acidic media and demonstrate long-term stability on fluorine-doped tin oxide (FTO) electrodes with the use of a proton-conductive Nafion membrane. Preliminary DFT analysis shows a possibility for a unique mechanism where O—O bond formation is spontaneous from $Fe^{IV} = O$;$Fe^{IV} = O$ state via radical coupling. While this study mostly introduces the Fe-triazolate as a new water oxidation catalyst and photocatalyst, a limited analysis of Mn, Co, and Cu doping at ~20% was attempted with the idea of altering the composition of the metal d-orbitals, pKa of metal-bound water/hydroxy ligands, and metal-based spin states. This limited screening of doping resulted in no improved performance.

Here, the MOF was synthesized by using the reported procedure with a slight modification, where instead of using iron(II) chloride, we use iron(II) sulfate.[8] Residual Cl^- ions might be detrimental for the WOC activity as Cl^- can be oxidized under WOC conditions. Cl^- ion can also block Fe-H_2O sites needed for catalyst activation. Thus, iron(II) chloride was substituted for iron(II) sulfate. The Fe-$Mn(ta)_2$ was synthesized by doping ~18% of $MnSO_4$ into reaction mixture. The structure of the $Fe(ta)_2$ and Fe-$Mn(ta)_2$ MOF was characterized by PXRD (Figure 1b) and the PXRD patterns of $Fe(ta)_2$ crystalline structures agree with the simulated PXRD patterns of the CCDC deposited structure. The electric conductivity of MOFs was measured with and without light using a custom-made device (Figure S1). $Fe(ta)_2$ and Fe-$Mn(ta)_2$ show the conductivity of 5.28×10^{-5} and 0.92×10^{-5} S cm^{-1}, respectively, which slightly increases under illumination.[8,11–13] This result is in good agreement with the earlier report for $Fe(ta)_2$ listing conductivity of 7.7×10^{-5} S cm^{-1},[8] while a more recent study reported better conductivity measured via a different approach (four probe measurement).[14] High conductivity was attributed to the presence of a 3D network of (Fe-N-N)∞ chains. Doping

with Mn decreases the conductivity. The FTIR spectrum of $Fe(ta)_2$ shows bands at 800–1400 cm^{-1} for the aromatic ring of the 1,2,3-triazolate ligand (Figure S2), and the absence of the N─H stretching at 3100–3500 cm^{-1} confirms the formation of the triazole-metal bond in the MOF.[8]

The light absorption property of $Fe(ta)_2$ is investigated using UV-Vis-NIR diffuse reflectance spectroscopy. The UV-Vis-NIR spectrum of $Fe(ta)_2$ is given in Figure S3a. The bandgap of the $Fe(ta)_2$ MOF was determined by transforming the UV-Vis-NIR diffuse reflectance spectra to Kubelka-Munk plots (details are given in the Supporting Information). The band gap for $Fe(ta)_2$ is found to be ~1.4 eV (Figure S3b), which is comparable with the ~1.28 eV band gap obtained by analysis of the Tauc plot and DFT-derived ~1.56 eV prediction.[14] In a three-electrode setup, using electrochemical impedance spectroscopy, the Mott-Schottky plots ($1/C^2$ vs. V) for the $Fe(ta)_2$ MOF with and without light were obtained (Figure S4). The positive slope of the Mott-Schottky plot for the MOF electrodes confirms its n-type semiconducting property. The x-intercept of the line of fit gives the flat-band potential, from which the conduction band (CB) potential can be calculated. The CB position for the $Fe(ta)_2$ MOF is found to be approximately -0.16 and -0.18 V versus NHE without and with light, respectively (Figure S4). The anodic shift of the valence band (VB) position in the presence of light indicates an increase in the amount of charge carriers after illumination, which enhances the photoelectrochemical properties of the photoanodes.[15] From the UV-Vis diffuse reflectance spectrum and Mott-Schottky plots, the positions of the CB and VB of the MOF are determined, as shown in Figure 1c. These energy bands suggest that, from a thermodynamic standpoint, the $Fe(ta)_2$ MOF serves as a viable photocatalyst for the water-splitting reaction (Figure 1c).

The $Fe(ta)_2$ and $Fe\text{-}Mn(ta)_2$ are further characterized by X-ray photoelectron spectroscopy (XPS). The XPS survey spectrum and high-resolution spectra of Fe 2p, N 1s, and C 1s of $Fe(ta)_2$ (Figure S5) confirm the presence of Fe, N, and C in the $Fe(ta)_2$ MOF surface. Similarly, the XPS survey spectrum and high-resolution spectra of Fe 2p, Mn 2p, N 1s, and C 1s of $Fe\text{-}Mn(ta)_2$ (Figure S6) indicate the presence of Fe, Mn, N, and C in the $Fe\text{-}Mn(ta)_2$ MOF surface. For $Fe(ta)_2$, the XPS peaks at 708.3 and 721.0 eV are assigned to Fe $2p_{3/2}$ and Fe $2p_{1/2}$ of Fe triazolate (peak separation of 12.7 eV), respectively, indicating that the iron is in a + 2 state. For $Fe\text{-}Mn(ta)_2$, the XPS peaks at 708.5 and 721.2 eV are attributed to Fe $2p_{3/2}$ and Fe $2p_{1/2}$ (peak separation of 12.7 eV), and XPS peaks at 642.1 and 654.0 eV are ascribed to Mn $2p_{3/2}$ and Mn $2p_{1/2}$ (peak separation of 11.9 eV), respectively, confirming the presence of bivalent Fe and Mn in $Fe\text{-}Mn(ta)_2$.[14,16] The presence of the bivalent iron is further confirmed by the significant intensity of the multi-electron excitation satellite peaks in the XPS spectra of $Fe(ta)_2$ and $Fe\text{-}Mn(ta)_2$. Further, the X-ray absorption near edge structure (XANES) and extended X-ray absorption fine structure (EXAFS) were carried out for $Fe(ta)_2$ MOF. These methods confirmed the Fe^{2+} oxidation state and overall MOF structure Figures S7, S8, Table S1. The Fe-K edge of $Fe(ta)_2$ MOF matches the FeO standard's position but has a different shape. EXAFS fits for $Fe(ta)_2$ match well it crystal structure with Fe coordination to N at ~1.94 and ~2.91 Å in the first and second coordination spheres and coordination to carbon at ~ 2.70 and ~3.88 Å in the second and third coordination sphere, material also has Fe-Fe distances at ~3.63 Å.[17] Interestingly, EXAFS fits improve when Fe-N coordination number is lowered from N = 6 to N = 5 indicating a possible ligand absence defects and it further enhances by addition of Fe-O distance at ~2.26 Å indicating possible water coordination at the defect sites, Figure S8, Table S1.

DFT calculations confirm the stability of the CCDC-deposited crystalline structure of $Fe(ta)_2$ (Table S2). The predicted band gap for the crystal with the DFT-optimized geometry turns out to be ~1.6 eV (vs. ~1.4 eV experimentally measured in this work and 1.56 eV previously reported).[14] We observe several bands slightly below the Fermi level down to approximately ~1.5 eV, while the remainder of the VB lies below ~ 2.5 eV. The electron density localized in the *d*-orbitals of Fe atoms accounts for nearly the entire density of states at or directly above the Fermi level (Figure 1d), while the CB has Fe as well as nitrogen localized states. Based on these results, we expect that the strongest optical excitations should involve mainly the *d*-orbitals of the Fe atoms and metal-to-ligand charge transfer states.

The O_2 evolution activity of the $Fe(ta)_2$ and $Fe\text{-}Mn(ta)_2$ were measured using cerium ammonium nitrate (CAN) as an oxidant in both H_2O and D_2O at $pH = 1$ (0.1 M HNO_3) by using a Clark electrode in aerobic conditions (Figures 2a,b and S10–S16). To determine the O_2 evolution rate, the mass of the $Fe(ta)_2$ and $Fe\text{-}Mn(ta)_2$ MOF varied from 0.1 to 1.0 mg while keeping the CAN concentration constant (400 mM, Figures 2a, S11, and S14). The kinetics of O_2 evolution were determined by considering the initial rate of O_2 evolution at different masses of the $Fe(ta)_2$ MOF (Figures S10, S12, and S15), which shows that the rate of evolution of O_2 was first-order in both H_2O and D_2O with a corresponding rates of ~26.3 μM mg^{-1} s^{-1} (Figure 2b) and ~12.2 μM mg^{-1} s^{-1} (Figure S13). Similarly, the O_2 evolution at different masses of the $Fe\text{-}Mn(ta)_2$ MOF is also first order with a rate of ~13.36 μM mg^{-1} s^{-1} (Figure S16). The rate of O_2 evolution in D_2O is lower than that in H_2O, demonstrating a kinetic isotope effect (KIE) of ~2.2. This can suggest that $Fe(ta)_2$ MOF oxidizes water through the WNA mechanism[18–21] or, alternatively, the rate-limiting step is proton-coupled electron transfer to create $Fe^{V}=O/Fe^{IV}=O$ species from where the radical coupling step is very fast, see DFT analysis below. Doping with different metal ions (Mn, Cu, and Co) in the $Fe(ta)_2$, MOF was found to decrease the O_2 evolution rate due to the decrease in the number of active Fe centers and changes in the local electronic structure (Figures S16 and S17).

To test if the $Fe(ta)_2$ is capable of photo-catalytic oxygen evolution as it is, 0.1 mg of the solid was dispersed in 0.3 mL of pure water in the Clark electrode at 20 °C without any co-catalyst or reducing/oxidizing agents. Under visible light irradiation (500 W) and stirring, the progression of O_2 evolution was recorded as a function of time (Figure 2c). The plot shows only a small amount of O_2 (Figure 2c). This indicates that $Fe(ta)_2$ alone does not have a considerable catalytic function of H^+ reduction, and impurities in the

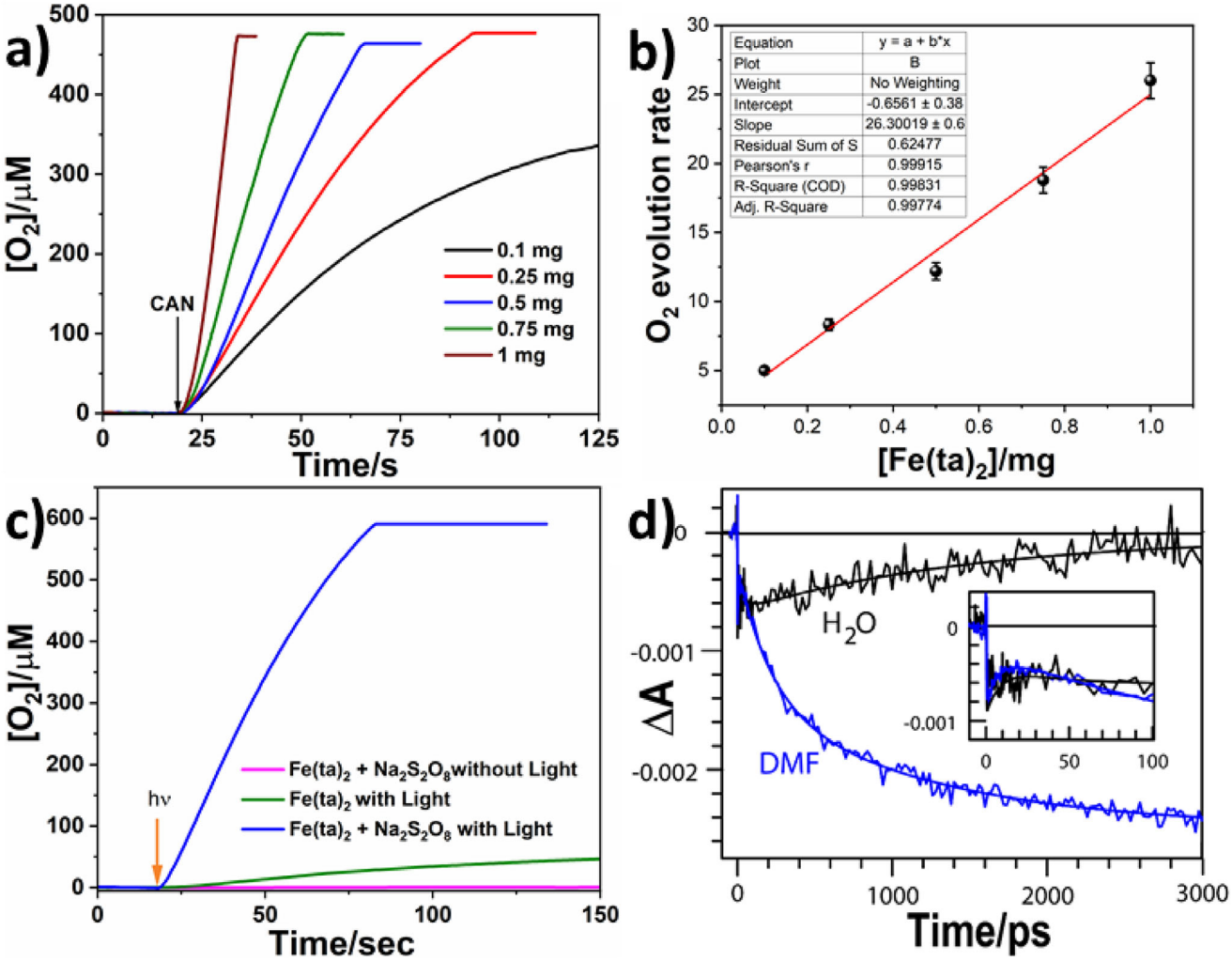

Figure 2. a) Chemical O_2 evolution at different concentrations of $Fe(ta)_2$ MOF in 0.1 M HNO_3 with 400 mM of CAN added at $t = 20$ s, b) Rate of catalytic O_2 evolution in H_2O at pH ~1, c) Photocatalytic O_2 evolution in water: $Na_2S_2O_8$ (0.1 M) and $Fe(ta)_2$ MOF (0.1 mg), without light, magenta curve; $Na_2S_2O_8$ (0.1 M) and $Fe(ta)_2$ MOF (0.1 mg), with light, blue curve; $Fe(ta)_2$ MOF (0.1 mg) in water with light, green curve, respectively, and d) Optical transient absorption spectra probed at 550 nm following the sample excitation at 390 nm for $Fe(ta)_2$ suspended in water and DMF.

buffer, as well as traces of Fe^{3+} ions, might serve as electron acceptors. Hence, the 0.1 M $Na_2S_2O_8$ was added as an external electron acceptor,[22] significantly increasing the photocatalytic O_2 evolution (Figure 2c). The total amount of $O_2 > 550$ μM was observed, which is comparable with the O_2 evolution by Ru-based molecular catalysts in the presence of $[Ru(bpy)_3]^{2+}$ as a photosensitizer at pH = 7.[4,23–25] The rate of O_2 evolution ~20.24 μM s^{-1} (Figure S18) is higher at pH = 7 photo conditions in comparison to results of chemical oxidation at pH = 1. Higher catalyst loadings were not explored as the oxygraph detection system saturated quickly.

Photo-induced dynamics in $Fe(ta)_2$ can be accessed by transient optical pump-probe absorption measurements. Figure 2d shows the absorption difference kinetics of suspension of $Fe(ta)_2$ microcrystals probed at 550 nm in water and dimethyl formamide (DMF) following excitation with ~250 fs long pulses at 390 nm. The experimental conditions and sample absorptions were kept the same for both solvents, so these kinetics could be directly compared. The major difference between these two solvents is the formation of a long-living state that causes a significant drop in absorption of the sample at 550 nm in the case of DMF. This state is formed with two lifetimes, ~0.2 ns (36%) and ~1.4 ns (38%), and has no indication of decay within the timeframe of the experiment (3 ns). The long lifetime of this state in DMF suggests that the state can be charge-separated and stabilized in the solid. Note that the best Fe-based photosensitizers can only demonstrate ~10 ps lifetimes of the charge-separated states, which are too short for efficient water oxidation.[26] Interestingly, for $Fe(ta)_2$ in water that state appears to be decaying with ~1.5 ns lifetime. Assuming that this state of $Fe(ta)_2$ has the same origin in both solvents, it suggests that there is an efficient competing mechanism in H_2O that quenches this state. The fact that the rise time of bleaching in DMF (1.4 ns) is similar to the decay time of bleaching in water (1.5 ns) indicates that this kinetic component in both solvents reflects the population rate of the state, but in H_2O there exists a mechanism that quenches this state much faster than

it is populated. This is also consistent with the low maximum amplitude of the photobleaching signal in H_2O. There is a hint of the rise time of this signal (~ 42 ps) in H_2O that could reflect this quenching process, but poor S/N prevents a definite determination of this kinetic component. In addition to the relatively slow photobleaching, $Fe(ta)_2$ in both solvents shows a fast-decaying photobleaching component (7.6 ps in DMF and 9 ps in H_2O), which forms immediately after excitation. The observed kinetics indicate the presence of at least three states that are formed consequently after excitation. The initial state is most probably a singlet excited state of the molecule that forms after absorption of light. This state evolves within 7–9 ps into a second state that has little effect on absorption changes detected at 550 nm. The second state then converts into a third state within 0.2–1.5 ns, causing a significant rise of photobleaching signal at 550 nm. Since this compound is known to be able to split water, one can assign the latter to a charge-separated state. In the case of DMF, this state does not decay within 3 ns, while in the case of water, it is quenched within a few nanoseconds. Recently, a similar system consisting of Fe-triazole in the form of $[Fe(Htrz)_2(trz)](BF_4)$ nanorods was reported to have ~ ps light-induced spin transition following the excitation at 266 nm, but data were not presented beyond ~100 ps time window.[27] The onset of high spin state was reported in ~5 ps to a few tens of ps time window depending on the pump light intensity. Thus, we cannot exclude that some of the observed transitions with rise time in ~ps correspond to low-spin to high-spin transitions in $Fe(ta)_2$ crystals. High spin states should be beneficial for charge separation and catalysis, as they resemble electronically more energetic states.

After multiple techniques have confirmed the photoactivity of $Fe(ta)_2$ and comparable catalytic activity of $Fe\text{-}Mn(ta)_2$, we proceeded with the fabrication of the photoanode by drop-casting of the ink prepared from powder $Fe(ta)_2$ MOF with 5% Nafion solution as a binder on the FTO electrode surface. These electrodes were tested by linear sweep voltammetry (LSV) and onset of catalytic current was demonstrated in 0.1 M HNO_3, Figure S19. The chronoamperometry technique was performed at $pH = 1$ (in 0.1 M HNO_3, 0.1 M $HClO_4$, and 0.1 M H_2SO_4) and by using a three-electrode system in an electrochemical cell (MOF-based photoanode with a Nafion membrane, Pt wire as a cathode, and Ag/AgCl reference electrode) at +1.4 V versus Ag/AgCl, (Figures 3a, b, and S20). Chronoamperometric curves of the $Fe(ta)_2$ MOF anode were collected without light (dark condition) in different electrolytes (0.1 M HNO_3, 0.1 M $HClO_4$, and 0.1 M H_2SO_4). Further, after ~2 h under the applied potential, the photo-assisted electrolysis with 1-min light on/1-min off for 20 min is recorded. $Fe(ta)_2$ shows a photo-electrocatalytic water oxidation current of 1.92 x 10^{-3}, 8.22 x 10^{-4}, and 1.19 x 10^{-3} Acm^{-2} with an applied potential of +1.4 V versus Ag/AgCl in 0.1 M HNO_3, 0.1 M $HClO_4$, and 0.1 M H_2SO_4 under illumination, respectively (Figures 3b and S20). The $Fe(ta)_2$ showed improved photo-electrocatalytic activity in 0.1 M HNO_3, this may be due to specific interactions between the nitrate ions and the Fe-based active sites within the MOF structure, although we do not yet fully understand the exact mechanistic reasons behind this improvement. Note, acid dependences were reported for Ru-based water oxidation catalysts earlier.[28] Further, the chronoamperometric curves of the $Fe\text{-}Mn(ta)_2$ MOFs were obtained in a similar way and photo-electrocatalytic current of 1.86 x 10^{-3} Acm^{-2} was demonstrated in 0.1 M HNO_3 (Figure 3b). The activity of $Fe(ta)_2$ MOF was also assessed with an applied potential of +1.23 V versus RHE (which is close to thermodynamic potential of water oxidation) in 0.1 M HNO_3. Under illumination, $Fe(ta)_2$ electrode shows a photo-electrocatalytic current of 6.2 x 10^{-4} Acm^{-2} (Figure S21). The $Fe(ta)_2$-photoanodes were tested for prolonged (>24 h) electrolysis at pH = 1 (0.1 M HNO_3) at +1.4 V versus Ag/AgCl (Figure S22). The enduring structural stability of the photoanode in an electrolyte solution and under the applied potential is undeniably critical for maintaining its electrocatalytic activity over prolonged periods of electrolysis. Photo-electrocatalytic activity of the $Fe(ta)_2$ MOF showed no significant change in current even after prolonged electrolysis. Furthermore, we conducted controlled potential electrolysis in a neutral solution (pH = 7) using $Fe(ta)_2$ MOF photoanode within the same three-electrode system. $Fe(ta)_2$ MOF shows a photocurrent of ~ 3.4 x 10^{-4} Acm^{-2} at an applied potential of +1.4 V versus Ag/AgCl in 0.5 M Na_2SO_4 when irradiated with visible light (Figure S23). We attribute this observed performance limitation to the reduced effectiveness of Nafion as a proton conductor under neutral pH conditions.

The structural stability of the materials plays a crucial role in assessing their performance and durability for water oxidation reactions. To investigate this, we measured the PXRD of the $Fe(ta)_2$ MOF after chemical oxidation with CAN and after photo-electrocatalytic water oxidation at pH = 1 (~24 h of chronoamperometry at +1.4 V versus Ag/AgCl) (Figure S24). The material retains its crystalline nature with a consistent peak position after post-water oxidation, indicating negligible structural changes or degradation of the material during the experiment. Growth of the intensity in some XRD peaks (at ~21 and 30° in Figure S24) after the prolonged exposure to electrolyte was observed in agreement with the earlier report.[14] We also carried out the scanning electron microscopy (SEM) of $Fe(ta)_2$, $Fe\text{-}Mn(ta)_2$, and $Fe(ta)_2$- after the photo-electrocatalysis (Figures S25 and S26). There is no significant change in the morphology of the sample even after 24 h of chronoamperometry (Figure S25a–d), suggesting the structural stability of the material during photo-electrocatalysis. Further, we performed the FTIR spectroscopy of $Fe(ta)_2$ before and after the photo-electrocatalysis. The FTIR spectra remained consistent after 24 h of chronoamperometry (Figure S27), further confirming the structural stability of $Fe(ta)_2$ during the photo-electrocatalytic process. This is in agreement with the earlier report on the high stability of $Fe(ta)_2$ in 1 M acid.[14]

The facile synthetic method for triazolate MOFs allows introducing other ions as additions to $Fe(ta)_2$. We determined that adding Mn^{2+} ions at ~18% preserves the photo-electrocatalytic activity, while other ions (Cu, Co) tested under limited conditions caused a decrease in the photo-catalytic current. However, the pure $Mn(ta)_2$ MOF has low stability in acid and dissolved when we attempted to assess its activity with CAN.

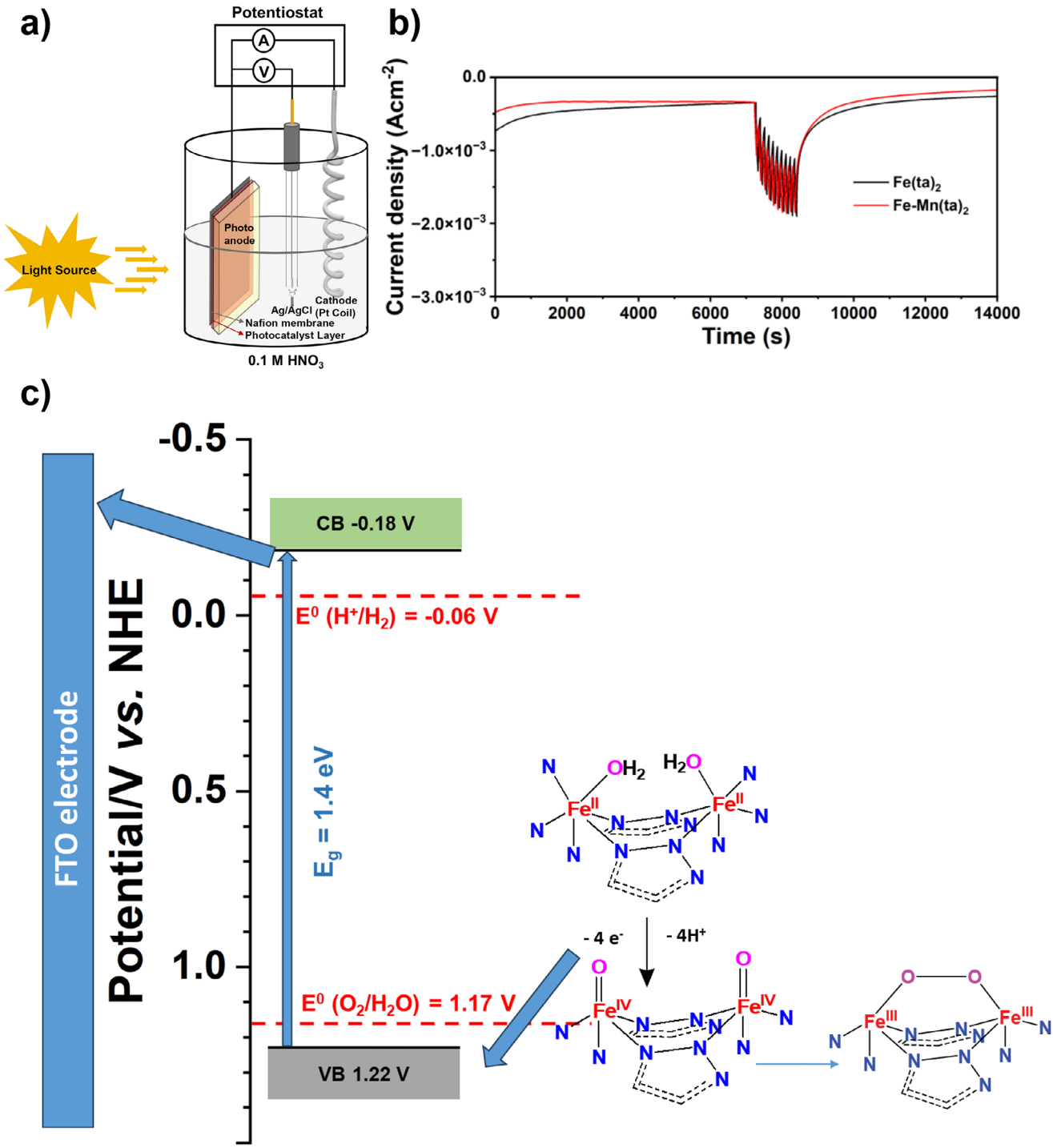

Figure 3. a) Three-electrode electrochemical setup with the $Fe(ta)_2$ and $Fe\text{-}Mn(ta)_2$ MOF photoanodes as the working electrodes confined by Nafion membrane, Ag/AgCl as the reference, and Pt-coil as the counter electrode. b) Chronoamperometry plot of the $Fe(ta)_2$ and $Fe\text{-}Mn(ta)_2$ photoanodes at pH = 1 (0.1 M HNO_3) with an applied potential of +1.4 V versus Ag/AgCl. c) Mechanism of dual photo-anode and water oxidation catalytic functions by $Fe(ta)_2$.

Metal-triazoles MOFs with triazolate and its derivatives as linkers and divalent metals have been reported as interesting materials with potential applications in clean energy (Figure 1).[8–10] This study uncovers the $Fe(ta)_2$ catalytic and photocatalytic ability in water oxidation (WOC) in acidic and neutral pH. Table S3 compares the performance of $Fe(ta)_2$ with other reported Fe-based water oxidation catalysts active at pH = 1. In chemically driven water oxidation, $Fe(ta)_2$ stands out with high stability and high TOF (Table S3). The high activity of chemically driven O_2 evolution, as well as the O_2 evolution under visible light with electron donor ($Na_2S_2O_8$) or biased electrode, highlights

the capabilities of $Fe(ta)_2$ MOF as a promising platform for light-driven water oxidation (Figure 2). High photocatalytic activity of $Fe(ta)_2$ indicates that this material has light-absorbing properties due to a suitably positioned bandgap and VB level. The photo-induced dynamics, characterized by the formation of long-living charge-separated states, provide insights into the underlying photocatalytic mechanisms. We attribute favorable light absorption properties to a low spin state of Fe centers in the $Fe(ta)_2$, as was demonstrated for some molecular Fe-based photosensitizers.[29]

High WOC activity of $Fe(ta)_2$ is likely due to the specific mechanism involving two closely positioned Fe centers, tentatively a defect site where Fe is coordinated with five nitrogen ligands and one water, Figure 3c. In chemically driven WOC, the $Fe(ta)_2$ activity per Fe center corresponds to turnover frequency (TOF) ~5 s^{-1}, and it is even higher in photo-driven WOC. However, as we hypothesize the defect with modified Fe ligation in $Fe(ta)_2$ to be an active center, the TOF of a true active center must be higher than this low-bound estimate. If we assume that same/similar centers are active in chemical and electrochemical WOC, we can relate the electrochemically addressable number of active centers to activity in chemical oxidation. In LSV, in the range of 1–2 V versus Ag/AgCl (Figure S19a), the number of active sites was estimated to be 3.91 x 10^{16} per mg of catalyst deposited onto the electrode. This assumes each center turns once during the LSV sweep in one electron process. This clearly gives the upper bound for the number of active centers. Comparing this number of centers to the chemically driven O_2 evolution rate of 26.3 μM s^{-1} mg^{-1} will result in TOF ~405 s^{-1}, which we consider a conservative estimate for the TOF of the active site (Table S3). Analyzing the active site further, we note that the negative charge of ligands should promote the oxidation of Fe to Fe^{V} needed to initiate O-O bond formation either via a water nucleophilic attack mechanism or via radical coupling[30] of two $Fe^{V}=O$ or $Fe^{IV}=O$ fragments. A close distance between two Fe centers (~3.6 Å) should facilitate coupling between the two neighboring Fe = O centers.[31] We created a preliminary DFT model where two Fe centers were coordinated with two bridging and six terminal (three to each iron center) triazoles, three of which (2 + 1 on two sides) were also protonated to keep the total charge of the model close to -1 (Table S5). This model represents the removal of the single bridging triazole, which can be readily envisioned for the surface or in the pore of the $Fe(ta)_2$ crystals. The model was propagated from $Fe^{II}-H_2O;Fe^{II}-H_2O$ configuration via proton coupled electron transfer (PCET) to $Fe^{IV}=O;Fe^{IV}=O$, which includes removal of $4e^-$ and $4H^+$ (Figure 3c). Curiously, $Fe^{IV}=O;Fe^{IV}=O$ state makes O—O bond spontaneously, and the highest energy PCET is attributed to the transition from Fe^{II} to Fe^{III} state in this model, which is in good agreement with the experimental onset potential and observed KIE. In future studies, this model will be embedded into the periodic structure of $Fe(ta)_2$, and alternative paths will be analyzed.

After we have discussed the origin of $Fe(ta)_2$ WOC and photo-driven WOC activity, we would like to reflect on its potential practical use as a photoanode. Based on the kinetic and photo-catalytic characterizations presented here, we believe $Fe(ta)_2$ opens a new avenue for research in artificial photosynthesis. First, we compare it with hematite, which is similarly scalable and has been extensively researched and optimized for use as a photoanode for artificial photosynthesis (Table 1). The highest theoretical photocurrent found for the hematite is ~ 12.6 x 10^{-3} $Acm^{-2,}$ and the highest photocurrent observed practically is 6 x 10^{-3} Acm^{-2}.[32–35] It was also found that due to increased photo-corrosion in acidic media, the hematite photoanodes are not stable in acidic conditions.[34,36–39] $Fe(ta)_2$ demonstrated photocurrent (~ 2 x 10^{-3} Acm^{-2}) comparable to the highest reported values of hematite-based photoanodes with no photoanode optimization.[40] Note, both systems require external bias to function as a photoanode, Table 1.[35] $Fe(ta)_2$ performance also exceeded reports for other photo-active Fe-based MOFs such as Fe_3O featuring MILs, which garnered significant attention for water splitting due to their high chemical and thermal stability.[6,11,41,42] It was noted that the Fe-based MOFs (i.e., Fe-MIL-101, Fe-MIL-126, Fe-MIL-100, Fe-MIL-88, and Fe-MIL-53) are capable of photocatalytic water oxidation under visible light when supplied with an electron acceptor.[42,43] Our earlier attempts to integrate the iron-based electrocatalyst $[Fe^{II}{}_4Fe^{III}(\mu_3\text{-}O)(\mu\text{-}\mathbf{L})_6]^{3+}$ (**L**H = 3,5-bis(2-pyridyl)pyrazole) reported as one of the fastest molecular WOC based on earth-abundant elements[44] into photoactive MIL-126 photoanode so far gave worse performance (~2 x 10^{-4} Acm^{-2}) at higher (+1.6 V vs. Ag/AgCl) applied potential and pH = 2.[45] Fe-based MOFs with $[Ru(bpy)(dcbpy)(H_2O)_2]^{2+}$[26] and $[Ru(tpy)(Qc)(H_2O)]^{+}$[4] as photo-electro catalytic water splitting systems at pH = 1 were reported, but despite integrated Ru-WOCs, they lag in performance, likely due to low electric conductivity, and the system is limited by a charge hopping mechanism. Table S4 gives more performance comparisons of $Fe(ta)_2$ to previously published systems. The increased current density plays a vital role in facilitating the efficient production of hydrogen gas during water splitting.

Overall, the realization of conducting Fe-based MOF as a material with dual functions of light absorption and high-rate WOC is an important development in the field of artificial photosynthesis. $Fe(ta)_2$ MOF's have promising catalytic characteristics for water splitting and renewable energy applications. Future optimization of performance and mechanistic studies will help to create efficient and sustainable photocatalytic systems for renewable energy production.

The study of Fe-triazolate ($Fe(ta)_2$) MOF as a catalyst for chemical, photochemical, and combinational photo-electrochemical water oxidation has shown exciting potential, particularly in comparison to other systems that use earth-abundant materials. $Fe(ta)_2$ MOF demonstrated desirable electronic properties, conducive to efficient light absorption and charge carrier generation. Catalytic studies showcased its effectiveness in promoting water-splitting reactions, both in acidic and neutral conditions. DFT demonstrated the possibility of a unique catalytic mechanism where O—O bond formation is possible from the coupling of two adjacent $Fe^{IV}=O$ fragments. Fabrication of $Fe(ta)_2$-based photoanodes exhibited sustained photo-electro catalytic activity,

Table 1: Comparison of the water oxidation photocurrent of different reported photoanodes during photo-electrocatalysis.

Name of the system	Potential (V vs. Ag/AgCl)	pH	Current density (Acm^{-2})	References
α-Fe_2O_3	0.9	13.6	1.16×10^{-3}	[32]
S@α-Fe_2O_3	1.1	14.0	1.42×10^{-3}	[46]
Ti@α-Fe_2O_3	1.1	13.3	3.1×10^{-3}	[47]
Sn@α-Fe_2O_3	1.3	13.6	3.3×10^{-3}	[48]
Pt@ α-Fe_2O_3@Co-Pi	1.1	13.1	4.32×10^{-3}	[40]
MIL-142 MOF with integrated $[Ru(tpy)(Qc)(H_2O)]^{+}$ WOC	1.4	1	1.6×10^{-3}	[4]
$Fe(ta)_2$	1.4	1	1.92×10^{-3}	This work
Fe-$Mn(ta)_2$	1.4	1	1.86×10^{-3}	This work

highlighting their stability and durability. Notably, promising results in photocatalytic water splitting underscore the versatility and efficiency of $Fe(ta)_2$ as a catalyst for renewable energy generation. These findings collectively emphasize the potential of $Fe(ta)_2$ MOF in addressing challenges in sustainable energy, paving the way for further research to optimize its catalytic performance and facilitate the development of scalable renewable energy technologies.

Acknowledgements

NSF, CHE-2155060 (Y.P.) supported this research. S.S. gratefully acknowledges support of the U.S. Department of Energy, Office of Basic Energy Sciences (Grant DE-SC0018239). P.G. is an independent contractor for ML LC. The authors thank Dr. O. Maximova and Mr. Hasan Tuncer for assistance with SEM measurements, Gabriel Bury for helpful discussions, and Dr. Dmitry Zemlyanov for the XPS measurements. We also thank Prof. Jianguo Mei for providing access to the electrochemical workstation and Dr. Palak Mehra for assistance with the Mott-Schottky plot measurements. All acknowledged scientists are affiliated with Purdue University. They also thank Dr. Ch. Chakraborty and Dr. P. K. Samanta from Birla Institute of Technology and Science, India, for the discussion of DFT modeling.

Conflict of Interests

The authors declare no conflict of interest.

Data Availability Statement

The data that support the findings of this study are available from the corresponding author upon reasonable request.

Keywords: Artificial photosynthesis · Density functional theory · Fe and Fe–Mn triazolate · Metal-organic frameworks · Photoanode · Water oxidation catalysis

[1] G. Segev, J. Kibsgaard, C. Hahn, Z. J. Xu, W.-H. (S.) Cheng, T. G. Deutsch, C. Xiang, J. Z. Zhang, L. Hammarström, D. G. Nocera, A. Z. Weber, P. Agbo, T. Hisatomi, F. E. Osterloh, K. Domen, F. F. Abdi, S. Haussener, D. J. Miller, S. Ardo, P. C. Mcintyre, T. Hannappel, S. Hu, H. Atwater, J. M. Gregoire, M. Z. Ertem, I. D. Sharp, K.-S. Choi, J. S. Lee, O. Ishitani, J. W. Ager, et al., *J. Phys. D Appl. Phys.* **2022**, *55*, 323003.
[2] M. Kumar, B. Meena, P. Subramanyam, D. Suryakala, C. Subrahmanyam, *NPG Asia Mater* **2022**, *14*, 88.
[3] T. Wydrzynski, S. Satoh, *Photosystem II: The Light-Driven Water:Plastoquinone Oxidoreductase*, Springer, Dordrecht, **2005**, *22*, 786
[4] J. Patel, G. Bury, Y. Pushkar, *Small* **2024**, *20*, e2310106.
[5] A. K. Singh, L. Roy, *ACS Omega* **2024**, *9*, 9886–9920.
[6] A. X. Zhu, J. B. Lin, J. P. Zhang, X. M. Chen, *Inorg. Chem.* **2009**, *48*, 3882–3889.
[7] W. Ouelleffe, A. V. Prosvirin, J. Valeich, K. R. Dunbar, J. Zubieta, *Inorg. Chem.* **2007**, *46*, 9067–9082.
[8] F. Gándara, F. J. Uribe-Romo, D. K. Britt, H. Furukawa, L. Lei, R. Cheng, X. Duan, M. O'Keeffe, O. M. Yaghi, *Chem.-Eur. J.* **2012**, *18*, 10595–10601.
[9] L. Sun, M. G. Campbell, M. Dincă, *Angew. Chem.* **2016**, *55*, 3566–3579.
[10] L. Sun, C. H. Hendon, S. S. Park, Y. Tulchinsky, R. Wan, F. Wang, A. Walsh, M. Dincă, *Chem. Sci.* **2017**, *8*, 4450–4457.
[11] M. Grzywa, R. Röss-Ohlenroth, C. Muschielok, H. Oberhofer, A. Blachowski, J. Zukrowski, D. Vieweg, H. A. K. Von Nidda, D. Volkmer, **2020**, *59*, 10501–10511.
[12] Z. H. Huang, N. H. Xie, M. Zhang, B. Q. Xu, *ChemSusChem* **2019**, *12*, 200–207.
[13] J. G. Park, M. L. Aubrey, J. Oktawiec, K. Chakarawet, L. E. Darago, F. Grandjean, G. J. Long, J. R. Long, *J. Am. Chem. Soc.* **2018**, *140*, 8526–8534.
[14] S. Khan, S. Chand, P. Sivasakthi, P. K. Samanta, C. Chakraborty, *Small* **2024**, *20*, 2401102.
[15] Y. Mei, T. T. Li, J. J. Qian, H. W. Li, Y. Q. Zheng, *J. Mater. Sci.* **2020**, *55*, 12864–12875.
[16] P.-Q. Liao, X.-Y. Li, J. Bai, C.-T. He, D.-D. Zhou, W.-X. Zhang, J.-P. Zhang, X.-M. Chen, *Chem.-Eur. J.* **2014**, *20*, 11303–11307.
[17] N. V. Bausk, S. B. Érenburg, L. G. Lavrenova, L. N. Mazalov, *J. Struct. Chem.* **1995**, *36*, 925–931.
[18] D. Moonshiram, V. Purohit, J. J. Concepcion, T. J. Meyer, Y. Pushkar, *Materials* **2013**, *6*, 392–409.
[19] S. Haschke, M. Mader, S. Schlicht, A. M. Roberts, A. M. Angeles-Boza, J. A. C. Barth, J. Bachmann, *Nature Comm.* **2018**, *9*, 4565.
[20] Z. Chen, J. Concepcion, X. Hu, W. Yang, P. Hoertz, T. Meyer, *Proc. Natl. Acad. Sci. USA* **2010**, *107*, 7225–7229.
[21] L. A. Gallagher, T. J. Meyer, *J. Am. Chem. Soc.* **2001**, *123*, 5308–5312.
[22] J. Patel, K. Majee, S. K. Padhi, *RSC Adv.* **2016**, *6*, 61959–61965.
[23] N. F. Khusnun, A. Arshad, A. A. Jalil, L. Firmansyah, N. S. Hassan, W. Nabgan, A. A. Fauzi, M. B. Bahari, N. Ya'aini, A. Johari, R. Saravanan, *J. Electroanal. Chem.* **2023**, *929*, 117139.
[24] J. Patel, G. Bury, A. K. Ravari, R. Ezhov, Y. Pushkar, *ChemSusChem* **2022**, *15*, e202101657.
[25] J. Patel, K. Majee, E. Ahmad, B. Das, S. K. Padhi, *Eur. J. Inorg. Chem.* **2017**, *2017*, 160–171.

[26] R. Ezhov, A. K. Ravari, M. Palenik, A. Loomis, D. M. Meira, S. Savikhin, Y. Pushkar, *ChemSusChem* **2023**, *16*, e202202124.
[27] M. Reinhard, K. Kunnus, K. Ledbetter, E. Biasin, D. B. Zederkof, R. Alonso-Mori, T. B. van Driel, S. Nelson, M. Kozina, O. J. Borkiewicz, M. Lorenc, M. Cammarata, E. Collet, D. Sokaras, A. A. Cordones, K. J. Gaffney, *ACS Nano* **2024**, *18*, 15468–15476.
[28] D. J. Wasylenko, C. Ganesamoorthy, M. A. Henderson, C. P. Berlinguette, *Inorg. Chem.* **2011**, *50*, 3662–3672.
[29] O. S. Wenger, *J. Am. Chem. Soc.* **2018**, *140*, 13522–13533.
[30] J. Patel, G. Bury, R. Ezhov, Y. Pushkar, *Artif. Photosynth.* **2025**, *1*, 174–187.
[31] R. Sarma, A. M. Angeles-Boza, D. W. Brinkley, J. P. Roth, *J. Am. Chem. Soc.* **2012**, *134*, 15371–15386.
[32] K. Sivula, F. Le Formal, M. Grätzel, *ChemSusChem* **2011**, *4*, 432–449.
[33] M. Barroso, S. R. Pendlebury, A. J. Cowan, J. R. Durrant, *Chem. Sci.* **2013**, *4*, 2724.
[34] V. B. Llorente, K. J. Jenewein, M. Bierling, A. Körner, A. Hutzler, A. Kormányos, S. Cherevko, **2023**, *127*, 19687–19697.
[35] B. K. Jha, S. Chaule, J. H. Jang, *Mater. Chem. Front.* **2024**, *8*, 2197–2226.
[36] T. Imrich, H. Krýsová, M. Neumann-Spallart, J. Krýsa, *J. Electroanal. Chem.* **2021**, *892*, 115282.
[37] J. Krýsa, A. Němečková, M. Zlámal, T. Kotrla, M. Baudys, Š. Kment, Z. Hubička, M. Neumann-Spallart, *J. Photochem. Photobiol. A Chem.* **2018**, *366*, 12–17.
[38] J. Krýsa, T. Imrich, Š. Paušová, H. Krýsová, M. Neumann-Spallart, *Catal. Today* **2019**, *335*, 418–422.
[39] G. F. Samu, C. Janáky, *J. Am. Chem. Soc.* **2020**, *142*, 21595–21614.
[40] J. Y. Kim, G. Magesh, D. H. Youn, J. W. Jang, J. Kubota, K. Domen, J. S. Lee, *Sci. Rep.* **2013**, *3*, 2681.
[41] J. P. Zhang, X. M. Chen, *J. Am. Chem. Soc.* **2008**, *130*, 6010–6017.
[42] Y. Horiuchi, T. Toyao, K. Miyahara, L. Zakary, D. D. Van, Y. Kamata, T. H. Kim, S. W. Lee, M. Matsuoka, *Chem. Comm.* **2016**, *52*, 5190–5193.
[43] L. Chi, Q. Xu, X. Y. Liang, J. D. Wang, X. T. Su, *Small* **2016**, *12*, 1351–1358.
[44] M. Okamura, M. Kondo, R. Kuga, Y. Kurashige, T. Yanai, S. Hayami, V. K. K. Praneeth, M. Yoshida, K. Yoneda, S. Kawata, S. Masaoka, *Nature* **2016**, *530*, 465–468.
[45] R. Ezhov, G. Bury, O. Maximova, E. Daniel Grant, M. Kondo, S. Masaoka, Y. Pushkar, *J. Catal.* **2024**, *429*, 115230.
[46] R. Zhang, Y. Y. Fang, T. Chen, F. L. Qu, Z. Liu, G. Du, A. M. Asiri, T. Gao, X. P. Sun, *ACS Sustainable Chem. Eng.* **2017**, *5*, 7502–7506.
[47] Z. B. Luo, T. Wang, J. J. Zhang, C. C. Li, H. M. Li, J. L. Gong, *Angew. Chem., Int. Ed.* **2017**, *56*, 12878–12882.
[48] J. J. Wang, Y. L. Hu, R. Toth, G. Fortunato, A. Braun, *J. Mater. Chem. A* **2016**, *4*, 2821–2825.

Manuscript received: June 21, 2025
Revised manuscript received: August 05, 2025
Accepted manuscript online: August 06, 2025
Version of record online: ■■, ■■